Available online at www.sciencedirect.com

ScienceDirect

Acta Materialia 79 (2014) 382–395

Acta MATERIALIA

www.elsevier.com/locate/actamat

Comparison between dislocation dynamics model predictions and experiments in precipitation-strengthened Al–Li–Sc alloys

Matthew E. Krug [a,*], Zugang Mao [a], David N. Seidman [a,b], David C. Dunand [a]

[a] Department of Materials Science and Engineering, Northwestern University, 2220 Campus Drive, Evanston, IL 60208, USA
[b] Northwestern University Center for Atom-Probe Tomography (NUCAPT), Northwestern University, Evanston, IL 60208, USA

Received 9 March 2014; received in revised form 15 June 2014; accepted 16 June 2014
Available online 17 August 2014

Abstract

Precipitate distributions were quantitatively measured by local electrode atom-probe (LEAP) tomography in several age-hardenable Al-based alloys to provide input to both analytical models and dislocation dynamics simulations of critical resolved shear strength, for comparison with experimentally measured Vickers microhardness values. The method of reconstructing precipitate-containing volumes from LEAP tomography, then importing these data to dislocation dynamics simulations, is explained in detail in the supplementary material available in the online version of this paper. Two alloys were studied: Al–2.9Li–0.11Sc at.% (Al–Li–Sc) and Al–6.3Li–0.07Sc–0.02Yb at.% (Al–Li–Sc–Yb). Heat treatment of these alloys produced nanometer-scale α'-$Al_3(Li, Sc, Yb)(L1_2)$ precipitates after isothermal aging at 325 °C. In some cases δ'-$Al_3Li(L1_2)$ shells were formed on these precipitates after subsequent isothermal aging at 170 °C. Dislocation dynamics results and experimental measurements were combined to define empirical strengthening superposition rules for the cases of contributions from: (i) Li in solid-solution plus α'-$Al_3(Li, Sc, Yb)(L1_2)$ precipitates; (ii) α'-$Al_3(Li, Sc, Yb)(L1_2)$ precipitates plus δ'-$Al_3Li(L1_2)$ shells in doubly aged Al–Li–Sc–Yb. Simulations of aged Al–Li–Sc overpredict the strength if a single dislocation is used, and underpredict the strength if instead a cooperative dislocation pair is considered. For simulations of dislocation pairs in Al–Li–Sc (single-phase precipitates), the precipitate bypass mechanism depends on the aging condition of the alloy. At peak age, precipitate shearing occurs mainly by pairs of closely spaced dislocations moving cooperatively. As overaging progresses, Orowan looping increasingly dominates and the distance between the leading and trailing dislocations increases. For dislocation pairs in doubly aged Al–Li–Sc–Yb with some core/shell precipitates, the measured and simulated strength values agree to within their uncertainties.

Keywords: Dislocation dynamics; Mechanical properties; Precipitation strengthening; Aluminum alloys; Atom probe tomography

1. Introduction

Al–Sc and Al–Li are two important classes of age-hardenable precipitation-strengthened alloys. Rare-earth (RE) element additions to Al–Sc alloys can result in increased strength at both ambient and elevated temperatures, due to the miscibility of Al_3Sc and Al_3RE [1], resulting in nanometer-radius α'-$Al_3(Sc_xRE_{1-x})$ precipitates upon aging at ~300 °C [2–14]. Lithium is a potent strengthening addition to Al alloys, because it provides solid-solution strengthening [15,16] and precipitation-strengthening by formation of $L1_2$-structured δ'-Al_3Li [15–27], while decreasing the alloy density [28,29]. Additional benefits accrue when Li additions are made to Al–Sc alloys aged at ~300 °C [30–37], resulting in an increase in both the volume fraction, φ, and number density, N_v, and a decrease in the mean radius, $\langle R \rangle$, of precipitates, which are of the type α'-$Al_3(Li, Sc)(L1_2)$ [38,39]. Further, with the application of a second heat treatment at ~200 °C, δ'-$Al_3Li(L1_2)$ can nucleate

* Corresponding author. Tel.: +1 614 726 2851.
E-mail address: matthewkrug6@gmail.com (M.E. Krug).

http://dx.doi.org/10.1016/j.actamat.2014.06.038
1359-6454/

Nomenclature

2D	two-dimensional
3D	three-dimensional
APB	anti-phase boundary
b	magnitude of Burger's vector
$\underline{b}$	the Burger's vector of a dislocation
C	factor to convert from hardness values to yield strength
C_i	(i are elements) concentration of element i
C_n	(n are counting numbers) constants in a polynomial
D1	the leading dislocation of a superdislocation pair
D2	the trailing dislocation of a superdislocation pair
DD	dislocation dynamics
D_χ	a term used to calculate $\tau_{size,\chi}$
E_χ	Young's modulus of phase χ
F_c	interaction force between a dislocation and a cylindrical inclusion
F_s	interaction force between a dislocation and a spherical inclusion
h_i	the "height" of a glide plane above the center of precipitate i
HV	Vickers microhardness
HV_{Al}	Vickers microhardness of pure annealed Al
IDD	inter-precipitate distance distribution
k	exponent used in calculating strengthening due to multiple contributions
LEAP	local electrode atom probe tomography
M	Taylor factor
m	exponent appearing in the expression for modulus mismatch strengthening
n	exponent used in calculating strengthening due to contributions from α'-Al_3(Li, Sc, Yb) precipitates and δ'-Al_3Li precipitates
MBD	model-based distribution
Nv	precipitate number density
N_χ	a term used to calculate $\tau_{size,\chi}$
$P_{\alpha/\beta}$	pressure exerted on the interface between the phases α and β
PSD	precipitate size distribution
$\langle R \rangle$	precipitate mean radius
$\bar{R}$	mean radius for circular cross sections of precipitates assuming a square array of precipitates having an LSW precipitate size distribution
R_c	radius of the core phase in a core/shell precipitate
RE	rare earth elements
r_i	distance from the center of precipitate i
R_i	radius of precipitate i
R_s	radius of the shell phase in a core/shell precipitate
T1	precipitated phase in the Al–Cu–Li system
TBD	tomography-based distribution
TEM	transmission electron microscopy
u	radial displacement distance
u_χ	radial displacement distance in phase χ
VASP	Vienna ab-initio simulation package
V_χ	fractional change in volume when matrix material transforms to phase χ
x	direction parallel to the original line-sense of a dislocation in a DD simulation
X_i	coefficients equal to the number density of obstacles i relative to the total number density of all obstacles, used for calculating strengthening due to multiple contributions
$x_{\max}$	boundary of the DD simulation in the x direction
y	direction normal to the original line-sense of a dislocation in a DD simulation
$y_{\max}$	boundary of the DD simulation in the y direction
z	direction normal to the glide plane in a DD simulation
α	fcc-Al phase
α'	$L1_2$ Al_3Sc-based precipitated phase
a_χ	lattice parameter of phase χ
β	exponent used in calculating strengthening due to multiple contributions
δ'	$L1_2$ Al_3Li-based precipitated phase
$\Delta\mu$	difference between the shear moduli of the matrix and precipitate phases
ΔHV_{Li}	strength increment due to dissolved Li
$\Delta\sigma_{coh}$	coherency strengthening increment due to lattice parameter mismatch
$\Delta\sigma_{mod}$	modulus mismatch strengthening increment
$\Delta\sigma_{norm}$	normalized strength increment, relative to pure Al
$\Delta\sigma_{Or}$	strength increment due to Orowan dislocation looping
$\Delta\sigma^*_{Or}$	strength increment due to Orowan looping in overaged Al–Sc–X alloys
$\Delta\sigma_{ord}$	order strengthening increment
$\delta\tau$	the increment in externally-applied shear stress in the DD model
$\Delta\tau^{\max}_{ext}$	shear stress increment from dislocation dynamics simulations
$\Delta\tau_{precipitate}$	calculated shear stress increment, from analytical strengthening models
ε_χ	constrained lattice parameter mismatch between matrix and χ phases
ϕ	precipitate volume fraction
γ_{APB}	antiphase boundary energy
$\gamma_{APB,\chi}$	antiphase boundary energy of phase χ
Γ	dislocation line tension
$\langle \lambda^{2D}_{e-e} \rangle$	mean edge-to-edge inter-precipitate distance
μ_χ	shear modulus of phase χ

υ_χ	Poisson's ratio of phase χ
ψ	angle between the glide plane and the vector from the precipitate center to the dislocation segment
ρ	ratio of shell radius to core radius: R_s/R_c
$\tau_{\alpha'}$	strengthening contribution from α'-Al_3(Li, Sc, Yb) precipitates
$\tau_{\delta'}$	strengthening contribution from δ'-Al_3Li precipiatates
τ_{disloc}	dislocation stresses due to all other dislocation segments
τ_{drag}	dislocation stresses due to viscous drag
τ_e	stress acting on an edge dislocation
τ_{ext}	an externally-applied shear stress
$\tau_{ext}^{\max}$	the maximum externally-applied shear stress
$\tau_{ext}^{\max,edge}$	the maximum externally-applied shear stress in a simulation for a dislocation (or cooperative dislocation pair) initially of pure edge character
$\tau_{ext}^{\max,screw}$	the maximum externally-applied shear stress in a simulation for a dislocation (or cooperative dislocation pair) initially of pure screw character
τ_i	critical resolved shear stress of a glide plane due to contribution i
τ_{obst}	stresses due to interactions between dislocations and obstacles
τ_s	stress acting on a screw dislocation
$\tau_{size,\chi}$	lattice parameter mismatch stresses acting on dislocations in the χ phase, near a core/shell precipitate
τ'	total critical resolved shear stress of a glide plane
τ_χ	a term used to calculate $\tau_{size,\chi}$
θ	the angle formed by the Burgers vector and the x-axis (the direction of the line-sense for the dislocation in its initial simulated configuration)
θ'	precipitated phase in the Al–Cu–Li system
θ''	precipitated phase in the Al–Cu–Li system

and grow on some of the α'-Al_3(Li, Sc)($L1_2$) precipitates, thus forming core/shell precipitates, with α'-Al_3(Li, Sc)($L1_2$) cores and δ'-Al_3Li($L1_2$) shells [30–31,34–37,39–41], and providing an additional strength increase.

A large body of literature exists on dislocation dynamics (DD) simulations, and various models that address the interactions between dislocations and obstacles in a wide variety of metals and microstructure types; see for example Refs. [42–52]. As described in the supplementary material, we use an extension of a two-dimensional (2-D) DD simulation by Mohles and coworkers [53–67] where segmented, self- and mutually-interacting dislocations interact with obstacles as they glide across a plane. This DD model allows for various dislocation–obstacle interactions: order/disorder stresses [55,60,63,65,66], lattice parameter mismatch stresses [54,56–58,63] and dislocation loops [67]. It can handle one or more partial or perfect dislocations of edge or screw character [54,57] as well as a variety of obstacle morphologies, spatial and size distributions and volume fractions. The simulation results were compared with experimental measurements of strengthening from Co precipitates in a Cu-based alloy, yielding satisfactory results for the prediction of peak strength, and a slight overestimate for overaged alloys [61,63]. As described in the supplementary material, we enhanced this original model by Mohles by considering both single-phase and core/shell precipitates and by taking into account elastic interactions due to shear modulus mismatch between precipitates and the matrix. We developed a methodology to incorporate precipitate sizes and spatial arrangements measured by local electrode atom probe tomography (APT) into the model.

Here, using precipitate microstructures experimentally measured by APT, we determine by DD the predicted yield stress for an Al–Li–Sc alloy (with a single population of α' precipitates) and an Al–Li–Sc–Yb alloy (with core/shell α'/δ' precipitates). These DD results are compared with experimental yield measurements derived from Vickers microhardness and with closed-form solutions for yield strength taking into account solid solution strengthening from Li and precipitation strengthening from α' and α'/δ' precipitates.

2. Experimental procedures

2.1. Aged alloys

Two alloys, Al–2.9 Li–0.11 Sc (hereafter, Al–Li–Sc) and Al–6.3Li–0.07Sc–0.02Yb (hereafter, Al–Li–Sc–Yb), were cast, homogenized at 640 °C and underwent age-hardening heat treatments to produce strengthening precipitates. In the following, unless noted otherwise, all compositions are given in at.%. Both alloys were aged at 325 °C, resulting in the formation of α'-Al_3(Li, Sc, Yb)($L1_2$) precipitates, and in some cases Al–Li–Sc–Yb was subsequently aged at 170 °C to produce δ'-Al_3Li($L1_2$), which surrounds some of the Al_3(Li, Sc, Yb)($L1_2$) precipitates, forming a shell on them. Details of these procedures, as well as chemical and microstructural analyses of the aged alloys by APT and transmission electron microscopy (TEM), and the

results of Vickers microhardness measurement throughout the aging sequence, are given in Ref. [38] for Al–Li–Sc and Refs. [39,40] for Al–Li–Sc–Yb.

2.2. Dislocation dynamics model

To model doubly aged Al–Li–Sc–Yb alloys with both single-phase α′-Al_3(Li, Sc, Yb)($L1_2$) and core/shell α′-Al_3(Li, Sc, Yb)($L1_2$)/δ′-Al_3Li($L1_2$) precipitates, an existing DD model created by Mohles [53] was extended in several ways. Firstly, precipitate arrangements are based on experimentally measured microstructures in one of two ways. In the first, referred to here as the model-based distribution (MBD), the precipitate size distribution (PSD) is measured by APT, and used to determine both the PSD and the spatial distribution of precipitates in the simulation. In the second, referred to here as the tomography-based distribution (TBD), the APT-measured precipitate sizes and three-dimensional arrangements are represented directly in the simulation, allowing preservation of the core and shell sizes, and spatial distributions of individual precipitates. To increase the size of a glide plane that can be simulated by the TBD method, the APT-measured volume is copied multiple times, and stitched together to form a larger volume. Before the stitching operation, each copy undergoes a series of linear transformations to eliminate periodicity in the glide plane, which is a planar slice through the assembled volume. These two procedures are described in detail in the supplementary material. While both the MBD and TBD methods were used to model Al–Li–Sc with single phase precipitates, only the TBD method was used to model doubly aged Al–Li–Sc–Yb with core/shell precipitates.

The original DD model [53] was further extended by introducing more complex expressions for dislocation–precipitate interactions. The original DD model included interactions for precipitates exhibiting a lattice parameter mismatch with the matrix, and antiphase boundaries (APBs) when sheared; the present research adds interactions due to shear modulus mismatch between precipitates and matrix. The present implementation also fully represents the interactions between dislocations and core/shell precipitates, where the core, shell and matrix phases all have different lattice parameters, APBs and elastic constants. The derivation of the new interactions is given in the supplementary material.

Here, we present the results of DD simulations of the critical resolved shear stresses throughout the precipitation aging sequence in singly aged Al–Li–Sc with single-phase α′-Al_3(Li, Sc, Yb)($L1_2$) precipitates, and of singly- and doubly-aged Al–Li–Sc–Yb. In the doubly-aged state, both single-phase and core/shell α′-Al_3(Li, Sc, Yb)($L1_2$)/δ′-Al_3Li($L1_2$) precipitates are experimentally observed, and simulated. These simulation results are compared with experimental Vickers microhardness measurements, as well as analytical expressions based on simplified assumptions.

3. Results

Table 1 shows experimental precipitate mean radii, $\langle R \rangle$, volume fractions, φ, and number densities, N_v, for each of the aging conditions studied by DD simulations. Also shown for each aging condition are the average two-dimensional (2-D) inter-precipitate distances (i.e., edge-to-edge inter-precipitate distances), $\langle \lambda_{e-e}^{2D} \rangle$, for α′-$Al_3$(Li, Sc, Yb)($L1_2$) precipitates. Table 2 shows three types of strength data for each of the aged alloys: (i) experimentally measured Vickers microhardness HV; (ii) calculated shear stress increments, $\Delta\tau_{precipitate}$, based on the precipitate characteristics, Table 1, physical properties values (reported in the supplementary material) and closed-form strengthening models, as described in Section 4.1; and (iii) shear stress increments, $\Delta\tau_{ext}^{max}$, determined from DD simulations. The Vickers microhardness measurements cannot be directly compared to calculated and simulated shear stress increments; the steps necessary to make this comparison are treated in Section 4. Values of the calculated stresses for the mechanisms that are predicted to be operative, as explained in Section 4.1, are in shaded cells and in bold print.

4. Discussion

4.1. Closed-form equations for strengthening

The strengthening mechanisms in our alloys are complex, as their origins include contributions from solutes (mostly Li) dissolved in the α(fcc)-Al matrix, as well as precipitation strengthening from α'-Al_3(Li, Sc, Yb)($L1_2$) formed at 325 °C, and from δ′-Al_3Li($L1_2$) precipitates when aging subsequently at 170 °C. Theoretical models for alloy strengthening by precipitates have been extensively developed [68–70]. In the case of coherent, ordered, misfitting precipitates, the alloy strength can be related to different types of dislocation interactions with the precipitates or with the precipitate-induced strain field in the surrounding matrix. Closed-form expressions for strengthening via these mechanisms have been successfully used to interpret strengthening in Al–Sc alloys [3,4,6,10,12,13,71], and they include order strengthening, modulus and coherency mismatch strengthening and Orowan strengthening (also called dislocation looping).

Order strengthening arises when a dislocation shears the precipitate as it glides past it. In the case of $L1_2$-ordered precipitates, the agents of deformation are dislocation pairs (similar to superdislocations in pure ordered structures): the leading dislocation introduces an APB as it passes through the precipitate, and a trailing dislocation restores order. This mechanism has been observed experimentally in both Al–Sc [6,10] and Al–Li [15,72,73] alloys. Theoretical predictions for the stress required to shear precipitates is based on a treatment of the dislocation pairs gliding

Table 1
Aging conditions and precipitate characteristics for simulated alloys.

Alloy	Aging treatment	Precipitate characteristics			λ_{e-e}^{2D}, 2-D inter-precipitate distance (nm)		
		$\langle R\rangle$ (nm)	ϕ (%)	N_v (10^{22} m^{-3})	LEAP tomographic reconstruction	MBD	TBD
Al–Li–Sc ($\alpha'(L1_2)$ only)	325 °C/0.16 h	1.45 ± 0.04	0.292 ± 0.002	19.4 ± 0.1	32 ± 20	42 ± 21	44 ± 24
	" /8 h	1.94 ± 0.05	0.557 ± 0.003	13.1 ± 0.1	39 ± 22	42 ± 21	42 ± 21
	" /24 h	2.30 ± 0.08	0.478 ± 0.003	8.2 ± 0.7	39 ± 19	50 ± 23	51 ± 24
	" /280 h	3.8 ± 0.2	0.484 ± 0.002	1.8 ± 0.2	79 ± 43	86 ± 42	101 ± 52
	" /1536 h	5.2 ± 0.2	0.506 ± 0.001	0.73 ± 0.16	145 ± 114	129 ± 64	133 ± 60
Al–Li–Sc–Yb	325 °C/8 h	2.44 ± 0.07 (α')	0.870 ± 0.001 (α')	11.9 ± 0.7 (α')	43 ± 24 (α')	–	47 ± 26 (α')
	325 °C/8 h	2.34 ± 0.05 (α')	0.820 ± 0.001 (α')	12 ± 2 (α')	40 ± 22 (α')	–	42 ± 22 (α')
	+ 170 °C/20 h	7.3 ± 0.5 (δ')	2.062 ± 0.001 (δ')	1.6 ± 0.5 (δ')		–	
	325 °C/8 h	2.73 ± 0.08 (α')	0.871 ± 0.0001 (α')	8.5 ± 0.6 (α')	44 ± 28 (α')	–	45 ± 24 (α')
	+ 170 °C/168 h	12.2 ± 0.3 (δ')	5.5 ± 1.2 (δ')	0.55 ± 0.09 (δ')		–	

through the precipitate field. The increment in alloy strength from order strengthening is given by [68]:

$$\Delta\sigma_{ord} = 0.81 M \frac{\gamma_{APB}}{2b}\sqrt{\frac{3\pi\varphi}{8}} \tag{1}$$

where M is the Taylor factor, γ_{APB} is the APB energy, b is the magnitude of the Burgers vector of a matrix dislocation, and φ is the volume fraction of the precipitated phase.

Modulus mismatch strengthening is due to elastic interactions between the dislocation and the precipitate, arising from the difference in elastic modulus between the matrix and precipitate phases. The increment in alloy strength is given by [68]:

$$\Delta\sigma_{\mathrm{mod}} = 0.0055 M(\Delta\mu)^{3/2}\left(\frac{2\varphi}{\mu_m b^2}\right)^{1/2} b\left(\frac{\langle R\rangle}{b}\right)^{\frac{3m-2}{2}} \tag{2}$$

where $\Delta\mu$ is the difference in the shear modulus between the matrix phase μ_m and the precipitate phase μ_p, $\langle r\rangle$ is the mean precipitate radius and m is a constant taken to be 0.85.

Coherency strengthening is due to the elastic interaction between a gliding dislocation and the strain field surrounding a coherent, misfitting precipitate. The alloy strength increment is given by [68]:

$$\Delta\sigma_{coh} = M\,2.6(\mu_m\varepsilon)^{3/2}\left(\frac{\langle R\rangle\varphi b}{\Gamma}\right)^{1/2} \tag{3}$$

where $\varepsilon \approx 2/3(\Delta a/a)$ is the constrained lattice parameter mismatch and Γ is the dislocation line tension, taken to be $\mu_m b^2/2$. Modulus and coherency strengthening mechanisms operate simultaneously, and so their net effect is a linear summation. These two mechanisms operate in series with order strengthening, and so it is the larger of these two contributions that governs the alloy strength in the case where precipitates are sheared by dislocations.

For sufficiently large precipitates, the shearing stress becomes larger than the stress required for the dislocations to bow around the precipitates by the Orowan mechanism, which then becomes the controlling yield mechanism. Therefore, it is the smaller of the Orowan stress and the shearing stress that is operative. The alloy strength increment due to Orowan looping is given by [69,70]:

$$\Delta\sigma_{Or} = M\frac{0.4}{\pi}\frac{\mu_m b}{\sqrt{1-\upsilon_m}}\frac{\ln\left(2\frac{\bar{R}}{b}\right)}{\langle\lambda_{e-e}^{2D}\rangle} \tag{4}$$

where υ_m is the Poisson's ratio of the matrix phase, $\bar{R} = 0.822\,\langle R\rangle$ is the mean radius for circular cross-sections of precipitates assuming a square array of precipitates having an LSW precipitate size distribution and the mean edge-to-edge interprecipitate spacing in a glide plane is given by [70]:

$$\langle\lambda_{e-e}^{2D}\rangle = (1.538\varphi^{-1/2} - 1.643)\langle R\rangle \tag{5}$$

In the analysis that follows, Eqs. 1–5 are used to model precipitation strengthening in the aged alloys.

4.2. Superposition of strengthening mechanisms

4.2.1. Strength superposition laws

Empirical relationships are commonly used to describe the superposition of multiple strengthening mechanisms. They typically take the form:

$$\tau_t = \left(\sum_i X_i\tau_i^k\right)^{1/k} \tag{6}$$

where τ_t is the total critical resolved shear stress of a glide plane, which has contributions τ_i from multiple strengthening mechanisms i [16,68,70], and X_i are coefficients equal to the number density of obstacles i relative to the total number density of all obstacles. In many strengthening laws, X_i are taken to be equal to unity. The exponent k in Eq. (6) varies from 1 (arithmetic sum corresponding to linear superposition) to 2 (Pythagorean summation), and experimental studies have led to the adoption of a range of values in these limits [68,74–75]. A k value of unity corresponds to

Table 2
Aging conditions, measured Vickers microhardness, and calculated and simulated strength of aged alloys.

Alloy	Aging Treatment	Vickers Micro-hardness *HV* (MPa)	Calculated $\Delta\tau_{precipitate}$ (MPa)							Simulated $\Delta\tau_{ext}^{max}$ (MPa)			
										1 dislocation		2 dislocations	
			Phase	$\Delta\tau_{coh}$	$\Delta\tau_{mod}$	$\Delta\tau_{coh}+\Delta\tau_{mod}$	$\Delta\tau_{ord}$	$\Delta\tau_{Or}$	Phase	TBD	MBD	TBD	MBD
Al-Li-Sc	325°C/0.16 h	697±16		4.7±0.1	23.8±0.2	28.5±0.2	**38±8**	65±2		78±2	82±2	37±1	40±1
	" /8 h	820±24		7.3±0.1	35.2±0.3	42.5±0.3	**53±11**	79±2		102±2	110±2	53±1	48±1
	" /24 h	797±33	α′	8.2±0.9	37.0±0.4	45.9±0.4	**50±10**	66±3	α′	97±2	84±2	44±1	40±1
	" /280 h	704±12		12.6±0.3	44.9±0.7	57.5±0.7	52±10	**48±3**		67±2	66±2	37±1	36±1
	" /1536 h	603±10		16.2±0.3	51.9±0.6	68.0±0.6	54±11	**39±2**		55±2	50±2	42±1	37±1
Al-Li-Sc-Yb	325°C/8 h	711±14	α′	4.5±0.1	29.5±0.2	34.0±0.2	**47±10**	94±3	α′			47±2	
	325°C/8 h + 170°C/20 h		α′	4.27±0.05	28.3±0.2	32.6±0.2	**45±10**	92±2	α′			56±2	
		893±34	δ′	2.2±0.1	26.1±0.5	**28.3±0.5**	19±4	72±6	δ′			22±1	
					--				α′+ δ′	--		62±2	--
	325°C/8 h + 170°C/168 h		α′	4.8±0.1	30.4±0.2	35.2±0.3	**47±10**	86±3	α′			53±1	
		960±45	δ′	4.7±0.5	49±5	**54±5**	30±7	90±13	δ′			33±1	
					--				α′+ δ′			69±3	

the case in which the strengthening effects of different obstacle types are independent [76], whereas a larger value represents cooperative strengthening [77].

In early DD simulations on mixtures of obstacles of varying strengths [78], it was found that for two types of weak obstacles, the net strength is given by a Pythagorean summation of the individual obstacle strengths ($k = 2$), while for two types of strong obstacles, the net strength was closer to the arithmetic sum ($k = 1$). For the case of a continuous rectangular distribution of obstacle strengths (i.e., all strengths occur with an equal frequency), a Pythagorean summation provided the best fit [78]. Finally, the contribution of a small number density of strong obstacles was found to have a large and non-linear effect on the strength of a glide plane populated with a high number density of weak obstacles: this corresponds to precipitation strengthening of a matrix already strengthened by solute atoms [78]. A more recent study reported on line-tension-based DD simulations of mixtures of point obstacles A and B, at relative number densities X_A and X_B, where A obstacles were unshearable and the strength of B obstacles varied from easily shearable to unshearable [79]. A variation on the empirical relationship, Eq. (6) was found to fit the data well: $\tau_p = X_A^{\beta/2}\tau_A^{\beta} + X_B^{\beta/2}\tau_B^{\beta}$ (where the factors X_i differ from unity); the exponent β ranged from 1 (shearable B) to 2 (unshearable B) [79]. Other recent line-tension-based DD simulations showed that for mixtures of many weak obstacles (for example, solute atoms) and few strong obstacles (e.g., precipitates), a superposition exponent of $k = 1$ holds when the number densities of the two obstacle types differs greatly, and transitions to $k = 2$ as the relative number of strong obstacles increases [80]. This is in agreement with a summary of the numerical work, in which a linear superposition was only found to be appropriate for cases where a small number of strong obstacles are distributed among a large number of weak obstacles [69].

Experiments on Cu-rich Cu–Au solid solutions strengthened by SiO_2 particles resulted in a superposition exponent of $k = 1.8$ [74,81]. In a review of experimental work on Ni-based superalloys, which are strengthened both by dissolved solute atoms in the matrix and by ordered, coherent precipitates, it was found that, taking the X_i to be unity, the value of the summation exponent $k = 1.23$ best fits the experimental data for superposing the matrix and precipitate strengths of alloys in the under- and peak-aged states [75]. For other systems with shearable precipitates, similar results were found for Ni-based superalloys [82,83], and also for Cu-rich Cu–Au solid solutions strengthened by coherent Co-rich precipitates having a lattice mismatch with the matrix [84]. In a comprehensive review of data on strengthening of Al–Li by δ′-$Al_3Li(L1_2)$, $k = 1.23$ also provided the best fit to those literature data which were deemed of high quality [16,85]. In two separate studies [86,87] on the Al–Cu–Mg alloy 2024, which is strengthened by both shearable and non-shearable precipitates, models capturing the hardening kinetics during aging and due to friction stir welding have used a combined approach in which strengthening by the two types of precipitates was added using a Pythagorean summation, and this result

was added linearly with other strengthening contributions, such as the solid-solution matrix and grain boundaries. Similarly, in an Al–Cu–Li alloy, the strengthening contributions from unshearable θ' and T1 precipitates were added using a Pythagorean summation, and the result was added to the contribution from the shearable θ'' precipitates with a strengthening exponent $k = 1.4$ [88].

4.2.2. Solid-solution and precipitation strengthening in Al–Li–Sc

The strength of the present alloys in the as-quenched state is due primarily to solid-solution strengthening. After aging at 325 °C, strengthening is due to both dissolved solutes and to α'-$Al_3(Li, Sc, Yb)(L1_2)$ precipitates. Finally, after double-aging of Al–Li–Sc–Yb, solid-solution strengthening, α'-$Al_3(Li, Sc, Yb)(L1_2)$ precipitates and also δ'-$Al_3Li(L1_2)$ precipitates all strengthen the alloy. To interpret the simulation results, it is first necessary to establish a superposition rule, such as Eq. (6), for adding the effects of dissolved solutes and precipitates. Physical parameters such as the APB energy, the lattice parameter and the shear modulus of α'-$Al_3(Li, Sc, Yb)(L1_2)$ precipitates are unknown, and have been estimated for the present simulations (details reported in the supplementary material). Therefore, predictions of strength in the under- and peak-aged conditions, which rely on these values, may not be reliable for establishing such a rule. The strength increment due to Orowan looping of precipitates in overaged alloys relies, however, only on measurable precipitate parameters (Eqs. (4) and (5)). By comparing the measured strength increment in aged Al–Li–Sc with the results of Eqs. (4) and (5), it is hence possible to determine the superposition exponent k in Eq. (6).

This approach necessitates the establishment of the quality of fit of Eqs. (4) and (5) for predicting strength in overaged Al–Sc-based alloys with small volume fractions of precipitates. Therefore, in Fig. 1 we compare their predictions to measured Vickers microhardness results from past studies on binary Al–Sc [6,10], ternary Al–Sc–RE (RE = Dy, Er, Gd, Y or Yb) [89,90] and Al–Sc–Zr [91] alloys. Al–Li–Sc data are plotted as well in Fig. 1 for comparison, but were not included in the analysis that follows. The normalized strength increment relative to pure Al is given by:

$$\Delta\sigma_{norm} = \frac{(HV_m - HV_{Al})}{C\Delta\sigma_{Or}} \tag{7}$$

where HV_m is the measured Vickers microhardness of an aged alloy, HV_{Al} is the value for 99.999% pure Al, measured to be 180 ± 4 MPa, and C is a factor to convert from hardness values to yield strength, usually taken as $C = 3$ for various alloy systems [92]. In Ref. [89], yield-strength measurements made during compression tests of a precipitate-strengthened Al–0.09 Sc–0.03 Er alloy were compared with Vickers microhardness results for a range of aging conditions. The Al–Li–Sc data from which we wish to define a strength superposition rule have average

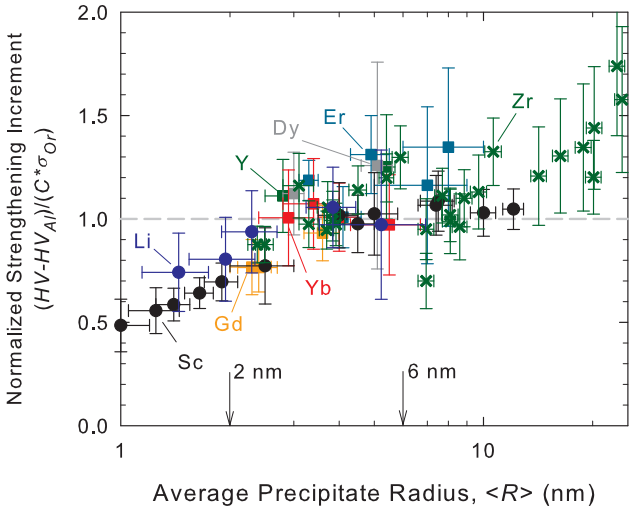

Fig. 1. Effect of average precipitate radius on strength increment due to precipitation, normalized to the strength predicted by the Orowan equation (Eqs. (4) and (5)) and the value $C = 2.88 \pm 0.07$. Data are for Al–Sc and Al–Sc–X alloys, where X is RE or Zr and is indicated on the figure. The horizontal dotted line corresponds to a strength increment that is exactly predicted by Eqs. (4) and (5). Data on Al–Li–Sc are also shown for comparison.

precipitate radii $\langle R \rangle$ in the range 2–6 nm. For precipitate radii smaller than 6 nm, and for the volume fraction of precipitates in Al–0.09 Sc–0.03 Er (0.49%), yield stress increments, $\Delta\sigma_{Or}$, are expected to be smaller than 100 MPa. Considering only those data in Ref. [89] that fit these criteria on precipitate radius and alloy strength, a conversion factor $C = 2.88 \pm 0.07$ is found, and is applied in the following analysis instead of the general value of $C = 3$. In Fig. 1 using this C value, the normalized strength increment $\Delta\sigma_{norm}$ is smaller than unity for all average precipitate radii below 2.8 nm. This is in approximate agreement with observations that, at average precipitate radii smaller than 2.1 nm, precipitate shearing, rather than Orowan looping, is the dominant strengthening mechanism [6,10]. At larger average radii, the data are scattered above and below unity, corresponding to a strength increment that is underpredicted and overpredicted by Eqs. (4) and (5), respectively. In the range between 2 and 6 nm, $\Delta\sigma_{norm}$ in Al–Sc–X alloys has an average value of 1.04 ± 0.15. In other words, the strength increment due to precipitates in overaged Al–Sc–X alloys, $\Delta\sigma^*_{Or}$, is given by:

$$\Delta\sigma^*_{Or}(\langle R \rangle) = 1.04 \pm 0.15 \times \Delta\sigma_{Or}(\langle R \rangle) \tag{8}$$

where $\Delta\sigma_{Or}$ is given by Eq. (4).

Using Eq. (8) with $C = 2.88 \pm 0.07$, we may solve for a superposition constant, k, which provides the best fit to the equation:

$$HV(\langle r \rangle) = HV_{Al} + \left\{ (\Delta HV_{Li})^k + [C\Delta\sigma^*_{Or}(\langle R \rangle)]^k \right\}^{1/k} \tag{9}$$

where $HV(\langle R \rangle)$ is the measured Vickers microhardness of the aged alloy, which contains precipitates of average radius $\langle R \rangle$, and ΔHV_{Li} is the Vickers microhardness due

to Li in solid solution. After aging, dissolved Sc and Yb are present only at very dilute concentrations so their solid solution effect can be neglected. The strength increment due to dissolved Li, $\Delta HV_{Li} = 47 \pm 10$ MPa, is found as the difference between the as-homogenized Vickers microhardness value in Al–2.9Li–0.11Sc, and that of a binary Al–0.12Sc alloy [38]. Using a non-linear least-squares regression on Eq. (15), k was found to be 0.94 ± 0.10. Performing the same analysis on Vickers microhardness data in aged Al–2.2 Mg–0.12Sc [93], which similarly has strength contributions from α'-Al_3Sc precipitates as well as dissolved Mg, yields a comparable value, $k = 0.95 \pm 0.03$. Using a regression on data combined from Al–2.9Li–0.11Sc and Al–2.2 Mg–0.12Sc, a value $k = 0.95 \pm 0.03$ is found. This is in approximate agreement with the analyses in Refs. [69,80], in which a linear superposition ($k = 1$) was predicted for the superposition of contributions from many weak obstacles (solute atoms) and fewer strong obstacles (precipitates). In the following analysis, the combined value, $k = 0.95 \pm 0.03$, is applied.

Measured Vickers microhardness values for aged Al–Li–Sc are plotted against average precipitate radius (Table 1) in Fig. 2. Three curves are also displayed in the figure, corresponding to Eq. (9): the gray lines are the maximum and minimum predicted Vickers microhardness values, propagating uncertainty in all parameters in Eq. (9) according to standard techniques [94], and the black curve is the mean predicted Vickers microhardness value. Eq. (9) predicts the Vickers microhardness of Al–Li–Sc well for the two largest average precipitate radii, but the predicted Vickers microhardness values for the three smallest average radii are too large, indicating that precipitate looping by the Orowan mechanism does not control the alloy strength at this precipitate size. Hardness for the smallest precipitate size is not shown on this figure, as the volume fraction of precipitates is significantly smaller than for the other four data points (Table 1) because the growth stage is still ongoing at this early aging state.

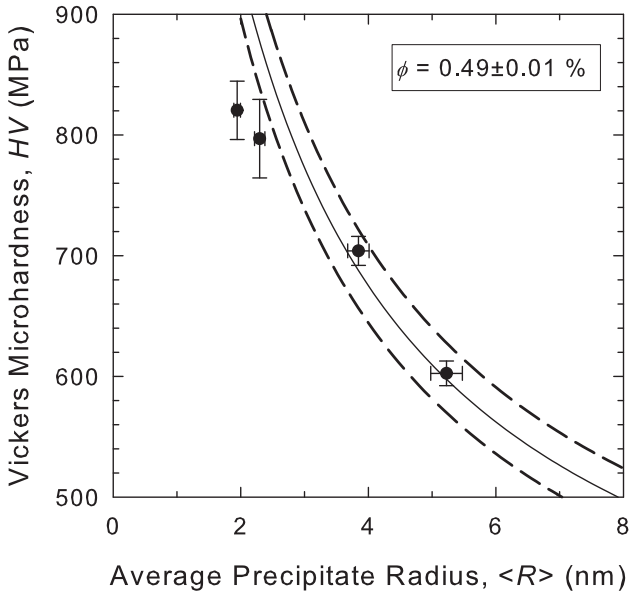

Fig. 2. Plot of Vickers microhardness of Al–Li–Sc vs. average precipitate radius, with predictions of Eq. (9) (curves) for Orowan strengthening shown with experimentally measured Vickers microhardness values (filled circles). The dashed black curves incorporate uncertainties propagated from all parameters in Eq. (9), and the continuous black curve is the mean predicted value.

4.3. Accuracy of DD predictions

4.3.1. Prior assessment of model accuracy and application to present alloy

In addition to the DD code used in the present research [53], dislocation–precipitate interactions have been studied recently using various DD programs [44,48,51,52,95–103]. While many DD studies have focused on interactions between one or several dislocations and a single precipitate [51,52,95–97,100,102,103], some studies have made quantitative predictions of yield stresses from simulations of dislocations gliding through an array of many precipitates, often with the aim of improving existing strengthening models, for example Refs. [48,61,66,99,101,104–106]. The DD code used in the present research (but without the modifications described in the supplementary material) was used to predict alloy strengths in a peak-aged Ni-based superalloy with either a monomodal or a bimodal PSD, depending on the heat treatment [66]. For both cases, LSW PSDs were assumed for each of the precipitate populations, whose mean radii and volume fractions were measured by TEM. The simulation results were comparable to experimental measurements, but underestimated the yield strength of the aged alloys (by 3% for the monomodal PSD or by 12% for the bimodal PSD) [66]. The same DD code was also used to simulate strengthening of Cu by lattice-mismatched Co precipitates for a range of precipitate sizes [61]. The precipitate volume fractions, mean radii and size mismatch had been determined in separate experimental studies [84,107]. Simulations of the peak-aged alloys, as well as models derived from studies using this same DD code [54,63], both compare favorably with the experimental results, although the simulation results for strongly overaged alloys deviate in either direction from the experimental values by ~10% [61].

In the present research, a conversion is used to compare strength increments calculated by closed-form solutions, and by dislocation dynamics simulations, to experimental Vickers microhardness measurements:

$$HV(\langle R \rangle) = HV_{Al} + \left\{ (\Delta HV_{Li})^k + [C \cdot M \cdot \tau]^k \right\}^{1/k} \quad (10)$$

where $C = 2.88 \pm 0.07$ and $k = 0.95 \pm 0.03$, as described above, and τ is the strengthening increment, either calculated by Eqs. 1–5, or equal to τ_{ext}^{max}, the result of a DD simulation. The hardness increment due to Li, ΔHV_{Li} is calculated as the difference between the measured Vickers microhardness of homogenized Li-containing and Li-free alloys: Al–2.9 Li–0.11 Sc (Al–Li–Sc) and Al–0.12 Sc

($\Delta HV_{Li} = 47 \pm 10$ MPa) [38], or Al–6.3Li–0.07Sc–0.02Yb (Al–Li–Sc–Yb) [39] and Al–0.048Sc–0.009Yb [38] ($\Delta HV_{Li} = 104 \pm 13$ MPa). Although the nominal Sc and Yb concentrations in Al–Li–Sc–Yb are greater than those in Al–0.048Sc–0.009Yb, due to the formation of primary grain boundary precipitates in Al–Li–Sc–Yb, the solute concentrations in the matrix are lower. The matrix composition in Al–Li–Sc–Yb was measured by APT to be Al–5.7Li–0.059Sc–0.008Yb [39], such that the matrix Sc + Yb concentration is only 100 at. ppm greater than in Al–0.048Sc–0.009Yb.

4.3.2. Simulation and experimental results for Al–Li–Sc

The Vickers microhardness of Al–Li–Sc, as measured experimentally [38], as calculated by Eqs. 1–5 and as determined by DD simulations, are shown in Fig. 3. The continuous black curve captures the experimental aging behavior throughout the heat treatment for many microhardness values [38], most of which are not individually reproduced here for clarity; measured microhardness values for the five simulated aging treatments are plotted along the curve. Calculated closed-form microhardness values, and DD-simulated microhardness values, are also plotted. Simulated values are shown for both the MBD method (single dislocations and cooperative dislocation pairs) and the TBD method (single dislocations and cooperative dislocation pairs) of creating a glide plane from APT reconstructions.

In Fig. 3, Vickers microhardness values based on closed-form precipitate strengthening models underpredict the measured Vickers microhardness values, but are within measurement uncertainty of the simulated Vickers microhardness values for under- and peak-aged states (0.16 and 8 h), excepting the data at 280 h. By contrast, in Fig. 3, the DD simulations using a single dislocation (label: 1 disloc.) consistently overpredict the measured Vickers microhardness and decrease with increasing aging time, because <R> is decreasing, and $\langle \lambda_{e-e}^{2D} \rangle$ is increasing (Table 1), consistent with an Orowan looping mechanism. The exceptions to this trend are the data at 0.16 h, for which the Vickers microhardness values are smaller than those at 8 h, due to the smaller volume fraction of α′-precipitates at this early aging time (Table 1). For 8 h aging, the DD simulations show that the single dislocation bows strongly around precipitates, but only the largest several precipitates are left ringed by an Orowan loop, i.e., most precipitates are sheared. After 1536 h aging, only the smallest several precipitates are not ringed by an Orowan loop and have been sheared. Although the simulated Vickers microhardness values for single-dislocation DD simulations always overpredict the measured Vickers microhardness values, at long aging times the simulated and experimental values nearly converge.

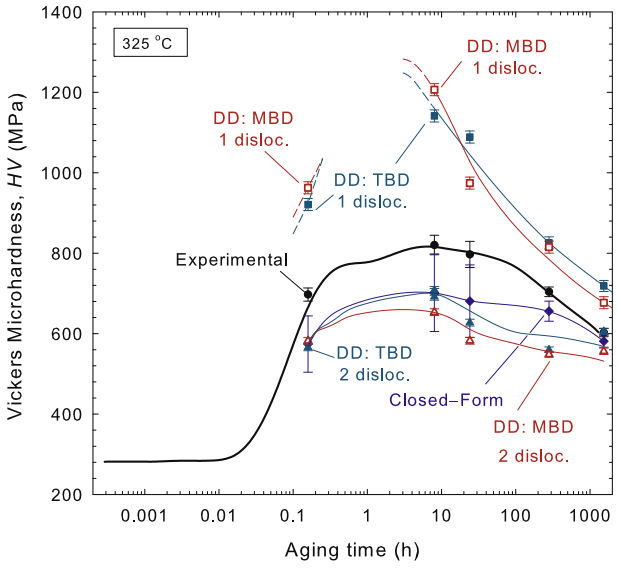

Fig. 3. Plot of Vickers microhardness of Al–Li–Sc vs. aging time, showing experimentally measured results [37], and values predicted by closed-form strengthening models and dislocation dynamics simulations.

As seen in Fig. 3, the DD simulations with a dislocation pair (label: 2 disloc.) consistently underpredict the measured Vickers microhardness. For 8 h aging, dislocations propagate as pairs, as shown in Fig. 4. Fig. 4a and b displays glide planes for Al–Li–Sc aged to 8 h, and Fig. 4c and d, with a different scale, are for 1536 h aging. In Fig. 4a and c, the dislocations are primarily of edge character (as indicated by the arrows next to the Burgers vector, $\underline{b}$, in the top-left insets), while in Fig. 4b and d the dislocations are primarily of screw character, corresponding to the initial dislocation type for each of these simulations. Intersections of α′-Al_3(Sc, Li) precipitates with the glide plane are indicated by blue disks, except when they are encircled by Orowan loops, in which case they are colored white to make them distinguishable. The leading and trailing dislocations, D1 and D2, are shown in black. Additional detail is given in Fig. 4c, in which a red square delineates a section that is expanded to greater magnification. In the magnified section, the precipitate intersections are shown at 75% of their actual radii to allow a clear visual distinction between the precipitates and the dislocations near them, and all precipitate intersections are shown as blue disks, including those that are encircled by dislocation loops.

For both edge and screw dislocations at 8 and 1536 h, several of the largest precipitates are surrounded by dislocation loops after the passage of the leading dislocation, D1, but these loops collapse as the trailing dislocation, D2, approaches, subjecting the dislocation loop to its stress field. Compared to 8 h aging, for 1536 h aging the distance between D1 and D2 is greater. Also, at 8 h aging, only the largest precipitates between D1 and D2 are encircled by an Orowan loop (most are sheared), whereas at 1536 h aging all but the smallest of the precipitates between them are surrounded by dislocation loops (few are sheared). This is, in effect, a transition from a predominantly shearing mechanism of precipitate bypass to a mechanism dominated by Orowan looping. For sufficiently large precipitate

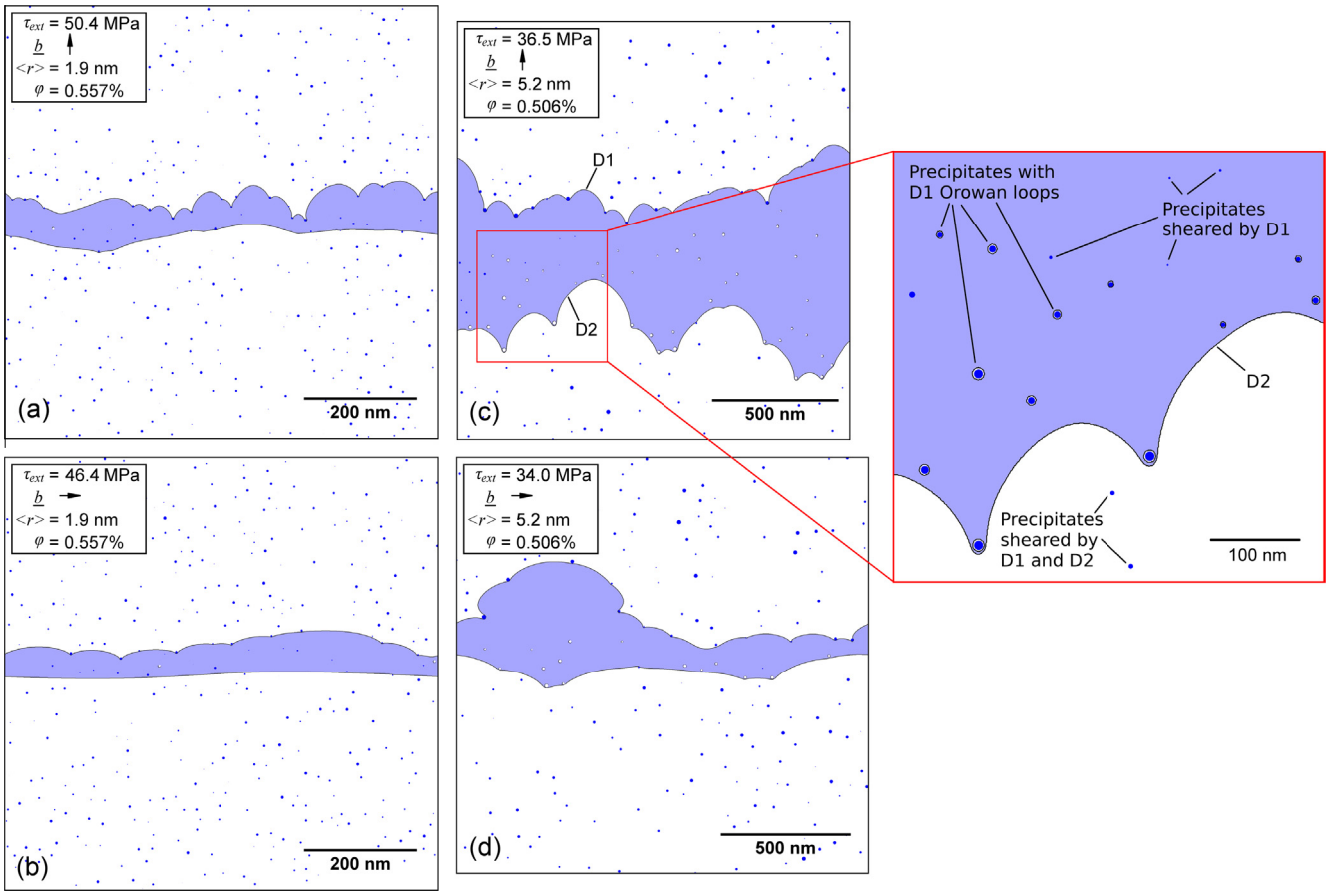

Fig. 4. Dislocation dynamics simulations of precipitates in Al–Li–Sc aged 8 h (a and b) and 1536 h (c and d), for edge (a and c) and screw (b and d) superdislocations, where glide planes are produced by the MBD method. Main parameters are given in the inserts.

radii, the distance between D1 and D2 would likely become very large, and hence the dislocations would be dissociated. At this point, the simulated Vickers microhardness values for single dislocations and for cooperative dislocation pairs should converge, as has nearly happened at 1536 h (Fig. 3). Capturing this behavior accurately would require larger datasets than those simulated here.

The discrepancy between measured and simulated Vickers microhardness values may be due to a number of factors. First, the number of precipitates modeled scales with the size of the glide plane. Further, the repeatability of the simulation result improves as the number of included precipitates is increased. In prior work using an earlier version of this DD model, it was shown that for a specified set of input parameters (obstacle volume fraction, mean radius, etc.), the scatter between simulation results of different obstacle fields was ~±6%, when simulating 500–1000 obstacles in the glide plane [53]. As discussed in the supplementary material, simulations of ~800 precipitates resulted in the same value (±6%). For time efficiency, we simulated a smaller number of obstacles, but no fewer than 200 precipitates, resulting in ±9% variability from the mean result for a given alloy and heat treatment.

Second, accurate treatment of the physical properties of the α′-precipitate phase is important for under- and peak-aged alloys, and these properties have been estimated using both first principles calculations and measured experimental data, as explained in the supplementary material. Uncertainties are encountered for the values of the lattice parameters and APB energies of the precipitate phases, which were calculated at 0 K conditions (see supplementary material). The effects of temperature on the calculated values for these properties can be estimated by considering their entropies, which have two contributions: configurational and vibrational. In this work, configurational entropy can be neglected because of the high degree of order in the $L1_2$ precipitate phase. We estimate that the vibrational entropy would account for differences in the calculated values on the order of 9% at room temperature, relative to their values at 0 K. In the case of lattice parameter, the effect of such an increase will be to either increase or decrease the lattice parameter mismatch with the matrix phase, depending on its sign. In the case of the APB energy the effect of a temperature-induced decrease will be to reduce the precipitates' efficacies for impeding dislocation motion. In both cases, a 9% error is on the order of other errors inherent in the simulation, and not considered to compromise the approach. Other thermally activated processes relevant to dislocation–precipitate interactions (i.e., climb) are not considered in this model, which is 2-D and used for moderate rates of deformation where creep is not appreciable.

To determine the sensitivity of the DD simulations (for deformation by cooperative dislocation pair motion) to the three most important physical properties – lattice parameter mismatch, ε, shear modulus mismatch, $\Delta\mu$, and anti-phase boundary energy, γ_{APB} – additional simulations were carried out in which each of these parameters were varied independently. The simulations were performed for the 8 h peak-aging treatment, using combined results from two edge and two screw dislocations, and a precipitate arrangement constructed by the TBD method. For the expected values of these parameters, τ_{ext}^{max} was 53 ± 1 MPa (Table 2). Increasing and decreasing ε and $\Delta\mu$ by 50% had little effect: varying ε over this range changed the maximum simulated shear stress, τ_{ext}^{max}, from 52 ± 1 to 55 ± 1 MPa, while varying $\Delta\mu$ changed τ_{ext}^{max} from 50 ± 1 to 55 ± 1 MPa. Varying γ_{APB}, by contrast, had a significant effect, as shown in Fig. 5. By varying γ_{APB} from 0 to 807 mJ m^{-2} (the expected γ_{APB} value is 0.461 J m^{-2}, see supplementary material) while maintaining ε and $\Delta\mu$ at their expected values, the simulated shear stress, τ_{ext}^{max}, increased from 9.5 ± 0.3 to 64 ± 1 MPa. For comparison, the results of closed-form solutions (Eqs. 1–5) for strength due to elastic interactions, $\tau_{coh} + \tau_{\mathrm{mod}} = (\Delta\sigma_{coh} + \Delta\sigma_{\mathrm{mod}})/M$, long-range ordered precipitates, $\tau_{ord} = \Delta\sigma_{ord}/M$, and Orowan looping bypass, $\tau_{Or} = \Delta\sigma_{Or}/M$, are plotted as dashed lines in Fig. 5. Of these, only τ_{ord} is a function of γ_{APB}. The DD simulation results are greater than τ_{ord} for small values of γ_{APB} due to contributions from elastic interactions, and are smaller than τ_{ord} for large values of γ_{APB} due to a gradual transition from precipitate shearing to Orowan looping bypass as the precipitates become more effective obstacles, as observed in Fig. 4.

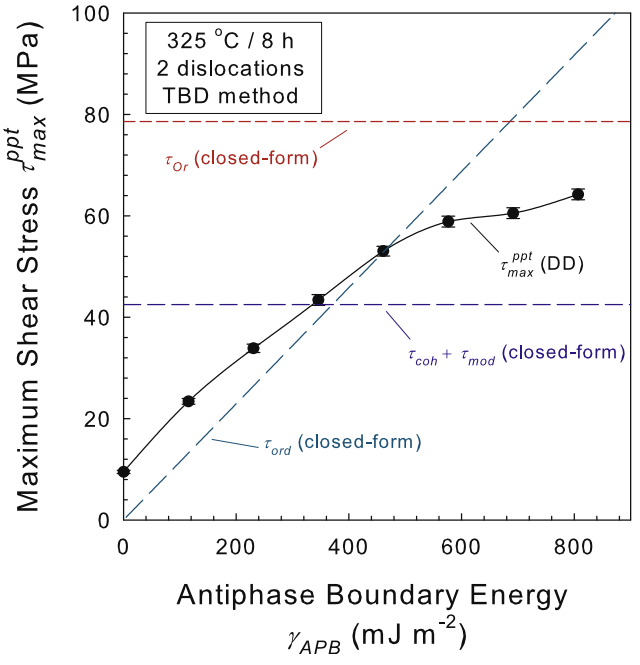

Fig. 5. Plot of maximum shear stress vs. anti-phase boundary energy for DD simulations of Al–Li–Sc aged 8 h at 325 °C.

The value of τ_{ext}^{max} that would bring DD simulations into agreement with measured Vickers microhardness values is 88 ± 3 MPa. This simulation result is not achieved by varying values for the precipitate properties within reasonable limits (Fig. 5). Two possibilities could account for the discrepancy. First, the value of τ_{ext}^{max} at $\gamma_{APB} = 0$ is small, 9.5 ± 0.3 MPa, compared to the closed-form solution for strength due to elastic interactions, $\tau_{coh} + \tau_{\mathrm{mod}} = 42.5 \pm 0.3$ MPa (Table 2). Shear modulus mismatch accounts for a majority of that value, 35.2 ± 0.3 MPa (Table 2), and therefore it is likely that the representation of that interaction in the simulations is inadequate. Second, the measured Vickers microhardness values of Al–Li–Sc all lie between the simulation results for one dislocation, and those for two dislocations (Fig. 3). Because the DD simulations are confined to a small representative area, on the order of 1 μm^2, the effects of local variations in grain size, grain orientation (and thus the Schmidt factor), dislocation source density and solute concentrations (and thus precipitate mean radius, volume fraction and number density) are not captured. It is likely that over macroscopic dimensions, the true precipitate bypass mechanisms comprise a mixture of the extreme cases represented by single-dislocations and cooperative dislocation pairs, as well as other complexities not represented by the model.

4.3.3. Simulation and experimental results for Al–Li–Sc–Yb

The measured, calculated and simulated Vickers microhardnesses for the high Li content Al–Li–Sc–Yb alloy are shown in Fig. 6. The continuous blue curve shows the experimental aging behavior throughout the 325 °C heat treatment, and the continuous red curve shows the experimental aging behavior for the 170 °C heat treatment, following 8 h of aging at 325 °C [39]. Experimentally measured Vickers microhardness values for the three simulated aging times are plotted along the curve as indicated. Using Eq. (10), calculated closed-form Vickers microhardness values and DD-simulated Vickers microhardness values are also plotted. Because the alloy is in a peak- or underaged state at the three aging durations considered, simulations were only performed for dislocation pairs, the expected deformation mechanism for alloys with $L1_2$-ordered precipitates. The TBD method was used for creating glide planes from APT reconstructions, for reasons described in the supplementary material. For the two doubly aged states, three simulations were performed for: (i) only the α′-Al_3(Li, Sc, Yb) precipitates that formed at 325 °C; (ii) only the δ′-Al_3Li phase that formed at 170 °C; and (iii) the full population of precipitates including α′-Al_3(Li, Sc, Yb) precipitates as well as core/shell α′-Al_3(Li, Sc, Yb)/δ′-Al_3Li precipitates. In case (ii), when the α′-Al_3(Li, Sc, Yb) cores are removed from the center of the δ′-Al_3Li shells, the anti-phase boundary energy is set to zero in the core region, and the effects of the lattice parameter and shear modulus mismatch between core and shell are neglected.

For the first point (8 h aging at 325 °C), the Vickers microhardness value from the Orowan strengthening closed-form model (709 ± 88 MPa) is the same as the

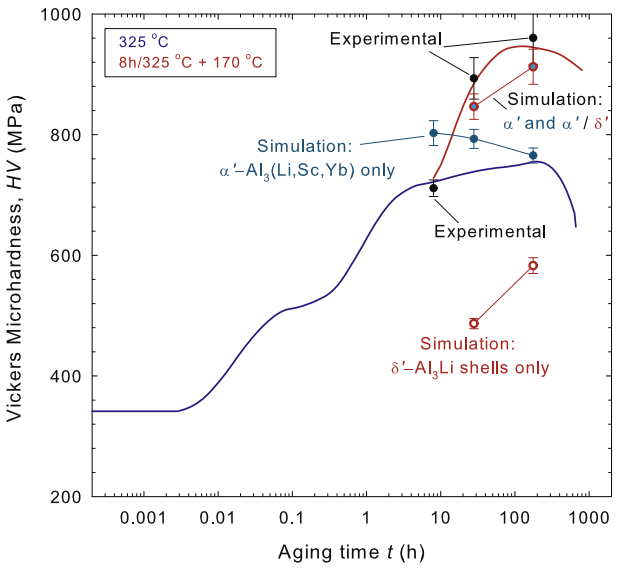

Fig. 6. Plot of Vickers microhardness of Al–Li–Sc–Yb vs. aging time, showing experimentally measured results [38], and values predicted by closed-form strengthening models and DD simulations. DD simulations on doubly aged alloys are decomposed into contributions from α′-Al_3(Li, Sc, Yb) and δ′-Al_3Li.

measured Vickers microhardness value (711 ± 14 MPa), while the DD simulation predicts a larger Vickers microhardness (803 ± 21 MPa, label: DD: TBD α′). This is contrary to the results in Al–Li–Sc, where the DD simulations and closed-form models both predicted values smaller than the experimentally measured Vickers microhardness. Simulations of the α′-Al_3(Li, Sc, Yb) precipitates after double-aging predict a trend of decreasing Vickers microhardness, for the case where the δ′-Al_3Li shells are assumed absent. However, these predicted Vickers microhardness values do not represent predictions of continued aging at 325 °C (blue curve), since aging durations greater than 8 h occurred at 170 °C and not 325 °C. Simulations of the Vickers microhardness contribution of δ′-Al_3Li in the two doubly aged conditions predict an increasing contribution, in accord with the increase in δ′-Al_3Li volume fraction (Table 1), and in close agreement with the closed-form value for order strengthening (Eq. (7)). DD simulations of the full population of precipitates (label: DD: TBD α′/δ′) result in Vickers microhardness values that are smaller than those measured experimentally, but that do capture the increase in Vickers microhardness due to the precipitation of δ′-Al_3Li shells on the α′-Al_3(Li, Sc, Yb) precipitates, which thereby become cores. Although the simulations results underpredict the experimentally measured values, the error bars in measurement and prediction are overlapping. From these simulations, a strength superposition law to account for the contributions of both the α′-Al_3(Li, Sc, Yb) and the δ′-Al_3Li precipitates, similar to Eq. (9), may be expressed as:

$$\tau_{precip} = \left(\tau_{\alpha'}^{n} + \tau_{\delta'}^{n}\right)^{1/n} \tag{11}$$

where τ_{precip} is the total strengthening contribution from all precipitates, $\tau_{\alpha'}$ and $\tau_{\delta'}$ are the contributions from the α′-Al_3(Li, Sc, Yb) and δ′-Al_3Li precipitates, respectively, and n is the superposition exponent, which is expected to be between 1 and 2. For the two doubly aged states simulated, a best-fit value of $n = 1.5 \pm 0.1$ was found. Hence, the total strength of the alloy is smaller than the linear sum of the contributions from α′-Al_3(Li, Sc, Yb) and δ′-Al_3Li, in agreement with models that indicate a transition from an exponent of unity (the case of solid-solution strengthening and precipitate strengthening) to 2 as the obstacle strengths and number densities become similar [69,78,80]. For doubly aged Al–Li–Sc–Yb, therefore, a superposition law that predicts the Vickers microhardness accounting for contributions from: (i) Li in solid solution, (ii) α′-Al_3(Li, Sc, Yb) precipitates formed at 325 °C and (iii) δ′-Al_3Li shells that form on the α′-precipitates at 170 °C, is given by:

$$HV = HV_{Al} + \left\{ \left(\Delta HV_{Li}\right)^{k} + \left[C \cdot M \cdot \left(\tau_{\alpha'}^{n} + \tau_{\delta'}^{n}\right)^{1/n} \right]^{k} \right\}^{1/k} \tag{12}$$

5. Summary

Two alloys – Al–2.9Li–0.11Sc at.% (Al–Li–Sc) and Al–6.3Li–0.07Sc–0.02Yb at.% (Al–Li–Sc–Yb) – were aged at 325 °C to produce strengthening α′-Al_3(Li, Sc, Yb) precipitates. Al–Li–Sc–Yb was additionally aged at 170 °C to produce core/shell α′-Al_3(Li, Sc, Yb)/δ′-Al_3Li precipitates. In specimens with single-phase precipitates, as well as ones with complex core/shell precipitates, microstructures were characterized using local electrode APT, the results of which were used as input to dislocation dynamics simulations, as explained in detail in the supplementary material. Using these simulations, strength predictions were compared with measured Vickers microhardness values, with the following results:

- A superposition law for adding strength contributions from Li in solid solution, and from α′-Al_3(Li, Sc, Yb) precipitates, was calculated based on prior aging hardness studies of Al–Sc–X alloys. The superposition law was then extended to account for additional strengthening by δ′-Al_3Li precipitates. Further conversions allow comparison between strengthening models or simulations, and Vickers microhardness (HV) measurements. The resulting expression is given by Eq. (12) where all parameters are available from literature, and $n = 1.5 \pm 0.1$ and $k = 0.95 \pm 0.03$ are exponents for superimposing strength contributions from the two types of precipitates, and from precipitates and Li in solid solution, respectively. The exponent k was determined from analysis of Vickers microhardness values in overaged Al–Li–Sc [38] and Al–2.2 Mg–0.12 Sc at.% [93], and the exponent n was determined from DD simulations of Al–Li–Sc–Yb.

- Simulations with one dislocation overestimate the Vickers microhardness of Al–Li–Sc, while simulations with two dislocations underestimate it. This is the case for both of the methods used to represent the measured microstructure. Predicted Vickers microhardness values based on simulations with one dislocation decrease with aging time, and hence with mean precipitate radius, corresponding to dislocation bypass by Orowan looping. Two-dislocation simulations indicate a transition from cooperative motion of a dislocation pair at early aging times, when most precipitates are sheared by the leading dislocation (D1), to longer aging times when most precipitates are bypassed by D1 leaving behind an Orowan loop. The trailing dislocation (D2) becomes increasingly distant from D1, as the deformation mechanism becomes less dominated by cooperative shearing by a dislocation pair, and instead more closely resembles Orowan bypass of the precipitates by independently acting dislocations. As this transition occurs, the results for one- and two-dislocation simulations nearly converge.
- Two-dislocation DD simulations of Al–Li–Sc where precipitate shearing is dominant are nearly insensitive to variations in the values used for the lattice parameter mismatch, ε, and for the shear modulus mismatch $\Delta\mu$ between precipitates and the matrix. By contrast they predict a near linear relationship between anti-phase boundary energy, γ_{APB} and maximum shear stress (and thus hardness). The discrepancy between measured Vickers microhardness values in Al–Li–Sc and the results of DD simulations may be due either to an inadequate treatment of the effects of shear modulus mismatch strengthening, or to an oversimplification in the deformation mechanism, which may be a mix of the cases of single-dislocation motion and cooperative dislocation pairs.
- Two-dislocation DD simulations predict reasonably well the Vickers microhardness of doubly aged Al–Li–Sc–Yb containing both single-phase α'-$Al_3(Li, Sc, Yb)$ precipitates and core/shell α'-$Al_3(Li, Sc, Yb)$/ δ'-Al_3Li precipitates. The simulation results allow the calculation of a superposition law for strengthening mechanisms in these alloys.

Acknowledgments

This research is supported by the U.S. Department of Energy, Office of Basic Energy Sciences (Dr John Vetrano, monitor) through Grant DE-FG02-98ER45721. The atom-probe tomograph was purchased with funding from the NSF-MRI (Grant DMR-0420532) and ONR-DURIP (Grant N00014-0400798, Dr Julie Christodoulou, grant officer) programs. We also gratefully acknowledge the Initiative for Sustainability and Energy at Northwestern (ISEN) for grants to upgrade the capabilities of the Northwestern University Center for Atom-Probe Tomography (NUCAPT). Professor V. Mohles (RWTH Aachen University, Aachen, Germany) is thanked for providing the source code for the dislocation dynamics simulations; Professor V. Mohles and Dr R.A. Karnesky (Sandia National Lab, Livermore, CA) are both thanked for numerous useful discussions about the code.

Appendix A. Supplementary data

Supplementary data associated with this article can be found, in the online version, at http://dx.doi.org/10.1016/j.actamat.2014.06.038.

References

[1] Harada Y, Dunand DC. Intermetallics 2009;17:17–24.
[2] Karnesky RA, VanDalen ME, Dunand DC, Seidman DN. Scripta Mater 2006;55:437–40.
[3] Knipling KE, Dunand DC, Seidman DN. Z Metallkunde 2006;97:246–65.
[4] Krug ME, Werber A, Dunand DC, Seidman DN. Acta Mater 2010;58:134–45.
[5] Marquis EA, Seidman DN. Acta Mater 2001;49:1909–19.
[6] Marquis EA, Seidman DN, Dunand DC. Acta Mater 2003;51:285–7.
[7] Novotny GM, Ardell AJ. Mater Sci Eng A 2001;318:144–54.
[8] Sawtell RR. Exploratory alloy development in the system Al–Sc–X. Berkeley, CA: University of California; 1988.
[9] Sawtell RR, Morris J. Dispersion strengthened aluminum alloys. Warrendale, PA: TMS; 1988. p. 409–20.
[10] Seidman DN, Marquis EA, Dunand DC. Acta Mater 2002;50:4021–35.
[11] Toropova LS, Eskin DG, Kharakterova ML, Dobatkina TB. Advanced aluminum alloys containing scandium. Amsterdam: Gordon & Breach; 1998.
[12] van Dalen ME, Dunand DC, Seidman DN. J Mater Sci 2006;41:7814–23.
[13] van Dalen ME, Seidman DN, Dunand DC. Acta Mater 2008;56:4369–77.
[14] Zakharov VV. Metal Sci Heat Treat 2003;45:246–53.
[15] Jeon SM, Park JK. Philos Mag A 1994;70:493–504.
[16] Nembach E. Prog Mater Sci 2000;45:275–338.
[17] Baumann SF, Williams DB. Metall Mater Trans A 1985;16:1203–11.
[18] Baumann SF, Williams DB. Acta Metall Mater 1985;33:1069–78.
[19] Hono K, Babu SS, Hiraga K, Okano R, Sakurai T. Acta Metall. Mater. 1992;40:3027–34.
[20] Messerschmidt U, Bartsch M. Mater Sci Eng A: Struct Mater: Prop Microstruct Process 1993;164:332–9.
[21] Miura Y, Matsui A, Furukawa M, Nemoto M. Plastic deformation of Al–Li single crystals. In: Aluminium–lithium alloys III. Oxford; 1986. p. 427–34.
[22] Noble B, Bray SE. Philos Mag: Phys Condens Matter: Defects Mech Prop 1999;79:859–72.
[23] Sanders TH, Starke EA. Acta Metall 1982;30:927–39.
[24] Schmitz G, Haasen P. Acta Metall Mater 1992;40:2209–17.
[25] Schmitz G, Hono K, Haasen P. Acta Metall Mater 1994;42:201–11.
[26] Williams DB. Microstructural characteristics of aluminum-lithium alloys. In: Sanders THJ, Starke EAJ, editors. Aluminum–lithium alloys, proceedings of the first international aluminum–lithium conference. Metallurgical Society of AIME; 1981. p. 89–100.
[27] Williams DB, Edington JW. Metal Sci 1975;9:529–32.
[28] Gasior W, Moser Z, Pstrus J. J Phase Equilib Diffus 1998;19:234–8.
[29] Levine E, Rapperport E. Trans Metall Soc AIME 1963;227:1204–8.
[30] Beresina AL, Kolobnev NI, Chuistov KV, Kotko AV, Molebny OA. Mater Sci Forum 2002;396–402:977–82.

[31] Berezina AL, Volkov VA, Ivanov CV, Kolobnev NI, Chuistov KV. Fizika Metallov I Metallovedenie 1991;2:172–80.
[32] Emigh RA. The aluminum–scandium–lithium–magnesium system as a potential source of superplastically formable alloys. Berkeley, CA: University of California; 1990.
[33] Emigh RA, Bradley EL, Morris JW. In: Lee EW, Kim NJ, editors. Light-weight alloys for aerospace applications II. Warrendale, PA: TMS; 1991. p. 27–43.
[34] Joh C, Yamada K. Mater Trans JIM 1999;40:439–42.
[35] Krug ME, Dunand DC, Seidman DN. Appl Phys Lett 2008;92:124107.
[36] Miura Y, Horikawa K, Yamada K, Nakayama M. Precipitation hardening in an Al–2.4Li–0.19Sc alloy. In: Aluminum alloys: their physical and mechanical properties, vol. 2; 1994. p. 161–68.
[37] Radmilovic V, Ophus C, Marquis EA, Rossell MD, Tolley A, Gautam A, et al. Nat Mater 2011;10:710–5.
[38] Krug ME, Dunand DC, Seidman DN. Acta Mater 2011;59:1700–15.
[39] Monachon C, Krug ME, Seidman DN, Dunand DC. Acta Mater 2011;59:3398–409.
[40] Monachon C, Dunand DC, Seidman DN. SMALL 2010;6:1728–31.
[41] Radmilovic V, Tolley A, Marquis EA, Rossel MD, Lee Z, Dahmen U. Scripta Mater 2008;58:529–32.
[42] Bako B, Weygand D, Samaras M, Chen J, Pouchon MA, Gumbsch P, et al. Philos Mag 2007;87:3645–56.
[43] Chang HJ, Gaubert A, Fivel M, Berbenni S, Bouaziz O, Forest S. Comput Mater Sci 2012;52:33–9.
[44] Fivel MC. C R Phys 2008;9:427–36.
[45] Huang MS, Zhao LG, Tong J. Int J Plast 2012;28:141–58.
[46] Ispanovity PD, Bako B, Weygand D, Hoffelner W, Samaras M. J Nucl Mater 2011;416:55–9.
[47] Kioussis NG, Ghoniem NM. J Comput Theor Nanosci 2010;7:1317–46.
[48] Monnet G. Philos Mag 2006;86:5927–41.
[49] Queyreau S, Monnet G, Devincre B. Acta Mater 2010;58:5586–95.
[50] Shin CS, Fivel MC, Verdier M, Robertson C. Mater Sci Eng – Struct Mater Prop Microstruct Process 2005;400:166–9.
[51] Takahashi A, Ghoniem NM. J Mech Phys Solids 2008;56:1534–53.
[52] Vattre A, Devincre B, Roos A. Intermetallics 2009;17:988–94.
[53] Mohles V. Philos Mag A 2001;81:971–90.
[54] Mohles V. Mater Sci Eng A 2001;319–321:206–10.
[55] Mohles V. Mater Sci Eng A 2001;309–310:265–9.
[56] Mohles V. Mater Sci Eng A 2001;319–321:201–5.
[57] Mohles V. Mater Sci Eng A 2002;324:190–5.
[58] Mohles V. Philos Mag Lett 2003;83:9–19.
[59] Mohles V. Computer simulations of dislocation glide in particle strengthened metal crystals; 2003.
[60] Mohles V. Mater Sci Eng A 2004;365:144–50.
[61] Mohles V. Dislocation dynamics simulations of particle strengthening. In: Continuum scale simulation of engineering materials: fundamentals – microstructures – process applications, vol. 17. Berlin: Wiley-VCH; 2004. p. 375–96.
[62] Mohles V, Fruhstorfer B. Acta Mater 2002;50:2503–16.
[63] Mohles V, Nembach E. Acta Mater 2001;49:2405–17.
[64] Mohles V, Rönnpagel D, Nembach E. Comput Mater Sci 1999;16:144–50.
[65] Mohles VN. Z Metallkunde 1999;90:896–900.
[66] Nembach E, Pesicka J, Mohles V, Baither D, Vovk V, Krol T. Acta Mater 2005;53:2485–94.
[67] Rong Z, Mohles V, Bacon DJ, Osetsky YN. Philos Mag 2005;85:171–88.
[68] Ardell AJ. Metall Trans 1985;16:2131–65.
[69] Brown LM, Ham RK. Dislocation-particle interactions. In: Kelly A, Nicholson RB, editors. Strengthening methods in crystals. Amsterdam: Elsevier; 1971. p. 9–135.
[70] Nembach E. Particle strengthening of metals and alloys. New York: Wiley-Interscience; 1996.
[71] van Dalen ME, Dunand DC, Seidman DN. Acta Mater 2005;53:4225–35.
[72] Furukawa M, Miura Y, Nemoto M. Trans Jpn Inst Metals 1985;26:225–9.
[73] Kalogeridis A, Pesicka J, Nembach E. Acta Mater 1999;47:1953–64.
[74] Lagerpusch U, Mohles V, Baither D, Anczykowski B, Nembach E. Acta Mater 2000;48:3647–56.
[75] Nembach E, Neite G. Prog Mater Sci 1985;29:177–319.
[76] Kocks UF, Argon AS, Ashby MF. Prog Mater Sci 1975;19:1–281.
[77] Koppenaal TJ, Kuhlmannwilsdorf D. Appl Phys Lett 1964;4:59–61.
[78] Foreman A, Makin M. Can J Phys 1967;45:511.
[79] Zhu AW, Csontos A, Starke EA. Acta Mater 1999;47:1713–21.
[80] Dong Y, Nogaret T, Curtin WA. Metall Mater Trans A 2010;41:1954–60.
[81] Lagerpusch U, Mohles V, Nembach E. Mater Sci Eng A 2001;319–321:176–8.
[82] Nembach E. Acta Metall Mater 1992;40:3325–30.
[83] Schänzer S, Nembach E. Acta Metall Mater 1992;40:803–13.
[84] Buttner N, Fusenig KD, Nembach E. Acta Metall 1987;35:845–54.
[85] Schlesier C, Nembach E. Acta Metall Mater 1995;43:3983–90.
[86] Genevois C, Deschamps A, Denquin A, Doisneau-cottignies B. Acta Mater 2005;53:2447–58.
[87] Khan IN, Starink MJ, Yan JL. Mater Sci Eng: A 2008;472:66–74.
[88] Gilmore D, Starke E. Metall Mater Trans A 1997;28:1399–415.
[89] Karnesky RA. Mechanical properties and microstructure of Al–Sc with rare-earth element or Al_2O_3 additions. Evanston, IL: Northwestern University; 2007.
[90] van Dalen ME. Microstructure and creep properties of Al–Sc alloys micro-alloyed with lanthanides (Yb or Gd) and transition metals (Ti or Zr). Evanston, IL: Northwestern University; 2007.
[91] Fuller CB, Seidman DN, Dunand DC. Acta Mater 2003;51:4803–14.
[92] Tabor D. Br J Appl Phys 1956;7:159–66.
[93] Marquis EA, Seidman DN, Dunand DC. Acta Mater 2003;51:4751–60.
[94] Bevington PR, Robinson DK. Data reduction and error analysis for the physical sciences: Mcgraw-Hill education. New York: McGraw-Hill; 2002.
[95] Shin CS, Fivel MC, Oh KH. J Phys Iv 2001;11:27–34.
[96] Shin CS, Fivel MC, Verdier M, Oh KH. Philos Mag 2003;83:3691–704.
[97] Yashiro K, Kurose F, Nakashima Y, Kubo K, Tomita Y, Zbib HM. Int J Plast 2006;22:713–23.
[98] Shin CS, Robertson CF, Fivel MC. Philos Mag 2007;87:3657–69.
[99] Queyreau S, Devincre B. Philos Mag Lett 2009;89:419–30.
[100] Takahashi A, Kawanabe M, Ghoniem NM. Philos Mag 2010;90:3767–86.
[101] Monnet G, Naamane S, Devincre B. Acta Mater 2011;59:451–61.
[102] Xiang Y, Srolovitz DJ. Philos Mag 2006;86:3937–57.
[103] Xiang Y, Srolovitz DJ, Cheng LT, Weinan E. Acta Mater 2004;52:1745–60.
[104] Fuchs A, Ronnpagel D. Mater Sci Eng A 1993;164:340–5.
[105] Bako B, Weygand D, Samaras M, Hoffelner W, Zaiser M. Phys Rev B 2008;78. 144104.
[106] Pretorius T, Nembach E. Acta Mater 2001;49:1971–80.
[107] Martin M. Überlagerung von Mischkristall- und Teilchenhärtung im System (CuAu)-Co [Ph.D. thesis]. Universität Göttingen; 1979.